International Journal of Microwave and Wireless Technologies

cambridge.org/mrf

Dual-band high isolation eight element MIMO antenna using self decoupling technique for 5G smartphone

Soumik Dey and Sukomal Dey

Department of Electrical Engineering, Indian Institute of Technology Palakkad, Kerala, India

Research Paper

Cite this article: Dey S, Dey S (2024) Dual-band high isolation eight element MIMO antenna using self decoupling technique for 5G smartphone. *International Journal of Microwave and Wireless Technologies*, 1–16. https://doi.org/10.1017/S1759078724001181

Received: 17 May 2024
Revised: 29 October 2024
Accepted: 9 November 2024

Keywords:
5G smartphone; antenna array; coupled resonator; dual-band; fifth generation (5G) communication; multiple input–multiple output (MIMO); self-decoupling

Corresponding author: Sukomal Dey; Email: sukomal.iitpkd@gmail.com

Abstract

Massive multiple input–multiple output (MIMO) antenna is required to meet the high data transmission rate in the current 5G and future 6G mobile communication. This paper presents a novel eight-port dual-band MIMO antenna operated within the 5G new radios N77 and N79 band. The designed MIMO incorporates a self-decoupling method to obtain high isolation of 22.96 and 25 dB at the two resonances 3.48 and 4.92 GHz, respectively. The basic antenna element consists of coupling between a staircase slot and a half-wavelength size loop branch. Additionally, an inverted U-shaped microstrip section is integrated with the radiating unit to serve the purpose of self-decoupling operation. The eight antennas are symmetrically located on the two narrow substrates (of size 5.8 × 150 mm^2) as a pair of four arrays. The narrow substrates make the metal rim of the 5.5′′ display mobile smartphone. The designed MIMO is practically realized and experimentally tested to validate the working mechanism. The envelope correlation coefficient and peak channel capacity are obtained as 0.174 and 35.5 bps/Hz in the lower frequency and 0.069 and 39.1 bps/Hz in the higher frequency.

Introduction

Since the onset of 4G and 5G, wireless communication has undergone significant advancements with high-speed broadband data streaming globally. Multiple input–multiple output (MIMO) antenna was developed to enhance channel capacity (CC) and data rates, and it also improves resilience against signal degradation from channel fading, enabling higher data throughput [1]. While various 4G MIMO antenna arrays operating in the Long-Term Evolution (LTE) bands (2.3/2.5 GHz) have been proposed [2–5], they often suffer from limitations such as poor isolation and large sizes, which restrict the number of MIMO elements in mobile devices. In recent years, the Federal Communications Commission has allocated various unlicensed bands above 3 GHz for 5G communication under the 3GPP framework, emphasizing high data rates (∼Gbps), ultrareliable low latency (<1 ms), and massive machine-type communication, supporting up to 10,000 Internet of Things (IoT) devices [6, 7]. Incorporating multiple antennas in the limited space of a system circuit board (SCB) leads to inevitable coupling, which negatively impacts MIMO performance by reducing diversity, deteriorating CC, and increasing specific absorption rate (SAR). Coupling arises from surface current propagation on the ground plane and space wave interaction in the near field [8, 9]. Techniques to improve MIMO isolation include decoupling structures and diversity methods. Surface wave is commonly attenuated using electromagnetic (EM) bandgaps, metamaterials, and defected ground structures [10–17], while space wave coupling is reduced with metamaterial absorbers and frequency-selective surfaces [18–20]. Additional methods like neutralization lines and LC networks create out-of-phase coupling paths [21–23]. However, these approaches often require large decoupling structures, making them impractical for mobile devices. Although spatial, polarization, and pattern diversity are effective alternatives, they present implementation challenges due to space constraints [24–26]. At 3.5 GHz, an eight-element MIMO array achieves over 15 dB isolation through pattern diversity stemming from varying electrical lengths of the radiators [27]. The self-decoupling from distinct patterns of three antenna pairs operating at 5.5 GHz enables the development of a 10-port massive MIMO antenna for 5G mobile terminals [28]. A low-correlation self-isolated MIMO array at 3.5 GHz features a T-shaped feed and stubs-loaded inverted U-shaped monopole radiator [29]. Various massive MIMO antennas designed for the LTE-42 band (3.4–3.6 GHz) exhibit isolation ranging from 10 to 17.5 dB [30–32], but these single-band designs do not meet the requirements of 5G multiband systems. A hybrid isolation improvement, consisting of decoupling capacitors and a T-shaped mode transformer, was demonstrated for suppressing all possible mutual coupling between inverted-F antenna (IFA) pairs within the n78 band [33]. Lumped capacitors were also embedded in the ground plane of the MIMO array to establish self-isolation for different antenna types, e.g., IFA, monopole, and loop antennas [34].

Additionally, composite lumped capacitors were introduced for independent frequency-selective decoupling in dual-band MIMO antennas [35]. Although the required area for the decoupling structure was significantly reduced, the complexity and tolerance of the lumped capacitors may limit their practical usage. Different dual-band MIMO arrays for the 5G mobile handset were showcased in references [36–45]. Three different antenna units of couple-fed open-end slot (OES) geometry are arranged over an 80×150 mm^2 area of an SCB to realize 8×8 MIMO array for the lower band (LTE 42/43) and 6×6 MIMO array for the higher band (LTE 46) [36]. Later designs employed T-shaped and L-shaped slots for dual-band operation, but these slot geometries on the SCB occupy significant space and are affected by the presence of liquid crystal display (LCD) screens, batteries, and human tissue [37, 38]. To address this issue, various dual-band MIMO arrays have been reported with antenna units integrated into the narrow side frame, which forms the metallic chassis of the smartphone. Common dual-band antenna units include folded monopoles and capacitively coupled open-loop branches [39–42]. Neutralization lines have been used in some of the dual-band MIMO arrays at the cost of design complexity, but isolation between adjacent antennas did not reach a satisfactory level [41, 42]. Obtaining high isolation simultaneously at the lower and higher operating bands without using an additional decoupling circuit is still considered to be a challenging task. In some of the works, multiband resonances are created from a combination of an OES in the ground plane of SCB and the monopole printed on the narrow side frame, but limitations of low isolation and high SAR value still exist [43–45]. To the best of the authors' knowledge, the OES and monopole loop branch together printed on the metal side-frame of a mobile smartphone for realizing dual-band antenna units of MIMO array have never been reported in earlier works.

This paper presents a novel eight-port dual-band MIMO array for sub-6 GHz 5G smartphones featuring high inter-element isolation. The radiating units of the array are designed entirely on the narrow metal side frames, leaving the entire space of the SCB for other electronic components. Each antenna unit consists of an open-end staircase slot and a directly fed parasitic open-loop branch. High isolation is achieved through a self-decoupling approach that incorporates an inverted U-shaped metal strip with each radiating element. The designed MIMO array resonates at frequencies of 3.5 GHz and 5 GHz, achieving a minimum measured isolation over 22.96 and 25 dB, respectively. The array exhibits low SAR values when analyzed with human hand and head phantoms. The "Design principle of dual-band MIMO" section discusses the construction and design principles of the MIMO element, while the "Simulation and measured results of eight-element MIMO" section details the simulated and measured return loss, isolation, and radiation characteristics of the proposed array. The "Diversity parameters and SAR analysis" section presents the effects of the user's hand and analyzes the SAR of the MIMO antenna. The "Effect of battery and LCD display" section presents the impact of the battery and display screen on the MIMO's performance, followed by the performance comparison of the suggested dual-band array with similar work reported previously.

Design principle of dual-band MIMO

Description of antenna geometry

Figure 1 shows the schematics of the proposed eight-port dual-band MIMO antenna, with a corresponding 3D perspective view, front view and side views (in $\pm y$ directions) presented separately. The architecture of the MIMO antenna is comprised of a SCB with a size of 150×75 mm^2 and two narrow metal frames (each of size 5.8×150 mm^2) along the long side edges. The SCB and metal frames are printed on FR-4 dielectric materials having thicknesses of 0.8 mm and 0.5 mm, respectively. The substrate used in this work has a relative permittivity of 4.4 and a dielectric loss tangent of 0.02. For the designed MIMO array, radiating elements 1–4 (denoted as Ant 1 to Ant 4) are placed on the long side edge at the right, whereas elements 5–8 (denoted as Ant 5 to Ant 8) are placed on the long side edge at the left (see Fig. 1[a]). Two clearance areas with each size of 8×75 mm^2 are left empty on the narrow sides of SCB to place the 2G/3G/4G or Global System for Mobile Communications (GSM) antenna.

The recommended MIMO antenna exhibits two resonances at 3.5 and 5 GHz with voltage standing wave ratio (VSWR) 3:1 bandwidth (BW) covering the LTE band 42 (3.4–3.6 GHz) and 5G new radio bands of N79 (4.4–5 GHz). The extended geometry of each MIMO element and the antenna's physical parameters are depicted in Fig. 1(c–d). In this work, the coupled resonator concept is implemented to obtain the dual resonance frequency of the antenna. The basic geometry comprises an OES with staircase configuration and a parasitic open-loop resonator (POLR) printed on two opposite faces of the metal side frame. The OES is energized using a U-shaped feed, whose parameters are properly optimized to obtain good impedance matching. One end of the POLR is connected with the U-shaped feed while the remaining end is shorted to the inner face of the narrow metal side frame using a plated through hole. The spacing between the two nearest antennas along long side edges is 16.9 mm or approximately 0.2 fractions of the wavelength at a lower resonant. For improving the isolation between antennas, an inverted U-shaped metal strip is gap coupled with POLR to realize the self-decoupling technique. The eight-port MIMO array is designed and numerically simulated using a full wave EM solver Ansys HFSS (High Frequency Structure Simulator). The final values of the physical parameters are mentioned in Table 1, where all units are given in millimeters.

Analysis of MIMO elements

To obtain better physical insight into the designed antenna, a single element of the MIMO (Ant 1) is placed at one corner of the large SCB. The resonance characteristic of Ant 1 is analyzed without the presence of a mutual coupling effect. Figure 2 depicts the layout of the single antenna element, which is designed based on the coupled resonance principle. The staircase OES and the POLR are energized using a U-shaped feed, which is connected to a microstrip line (printed on the back face of SCB) using a metal rod of diameter d_v. The SMA connector is attached to the microstrip line with a characteristic impedance of 50 Ω to launch the EM signal into it. In the proposed architecture, the slot mode of OES and patch mode of POLR are combined to realize the dual frequency operation. For the single MIMO element, the magnitude of the simulated reflection coefficient ($|S_{11}|$) is shown in Fig. 3(a). The antenna resonates at 3.5 and 5.02 GHz with return losses of 22.32 and 22.68 dB, respectively. The VSWR 3:1 BW (which is equivalent to $|S_{11}| = -6$ dB) of the antenna covers the frequencies 3.42–3.56 GHz and 4.92–5.12 GHz. Figure 3(b) presents the variation in the antenna's realized gain and total efficiency over the two bands. The gain and efficiency of the antenna are 2.68 dBi and 41.8% at the first resonant of 3.81 dBi and 47.4% at the second resonant. Figure 3(b) also reveals the sharp roll-off in the realized gain

https://doi.org/10.1017/S1759078724001181 Published online by Cambridge University Press

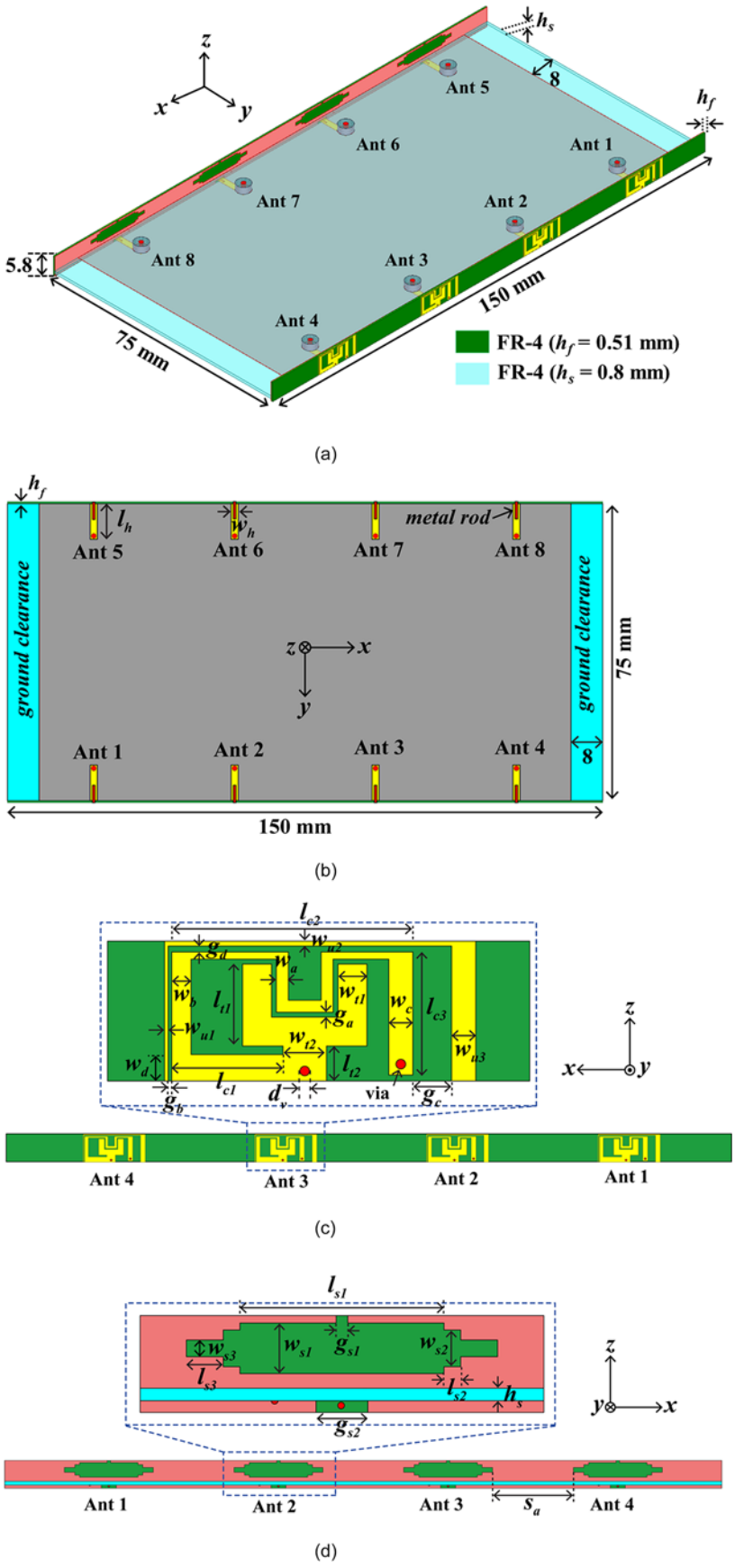

Figure 1. Architecture of the dual-band massive eight-port MIMO antenna (a) 3D isometric view (b) front view of system circuit board (c) front and rear view of metal frame.

https://doi.org/10.1017/S1759078724001181 Published online by Cambridge University Press

Table 1. Parametrically optimized dimensions of each antenna unit of the proposed dual-band MIMO array in millimeter

l_{c1}	l_{c2}	l_{c3}	w_{u1}	w_{u2}	w_{u3}	w_{t1}	w_{t2}	w_a	w_b	w_c	w_d	g_a	g_b	g_c
4.6	9.98	5.1	0.15	0.2	1	1.2	1.8	0.5	0.8	1	1.1	0.2	0.15	1.6
g_d	d_v	l_{t1}	l_{t2}	l_{s1}	l_{s2}	l_{s3}	w_{s1}	w_{s2}	w_{s3}	g_{s1}	g_{s2}	S_a	h_s	h_f
0.25	0.4	3.4	1.45	12.2	1	2.2	3.03	2.2	1	0.7	3.1	16.9	0.8	0.5

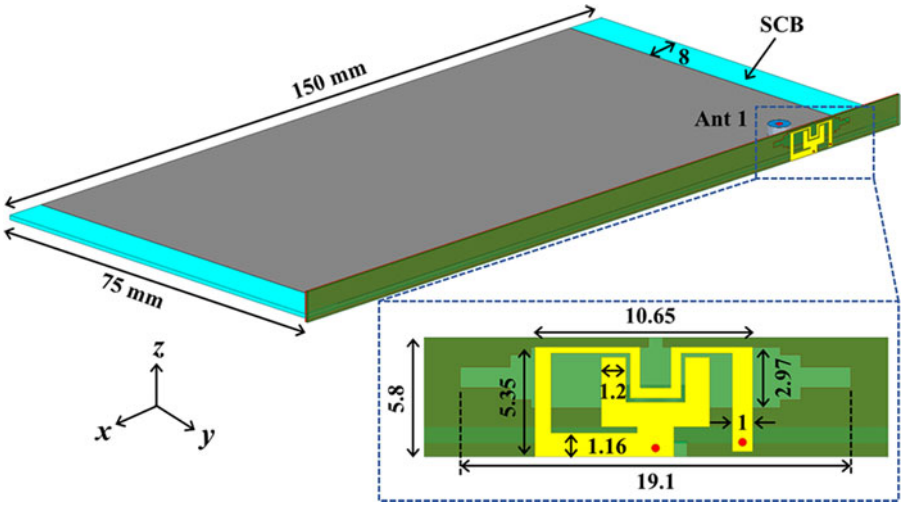

Figure 2. Schematic of the single MIMO element and its extended view on the SCB without the presence of mutual coupling effects from other antennas.

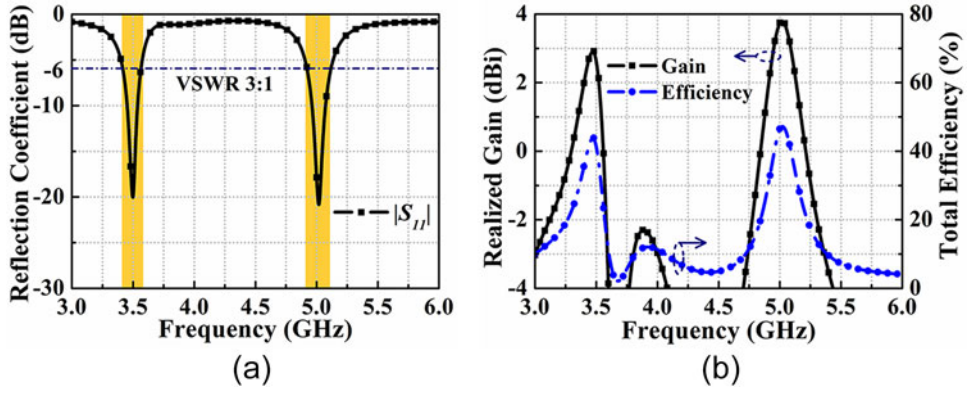

Figure 3. Simulated (a) retrun loss (b) gain and total efficiency variation of single antenna element on the SCB.

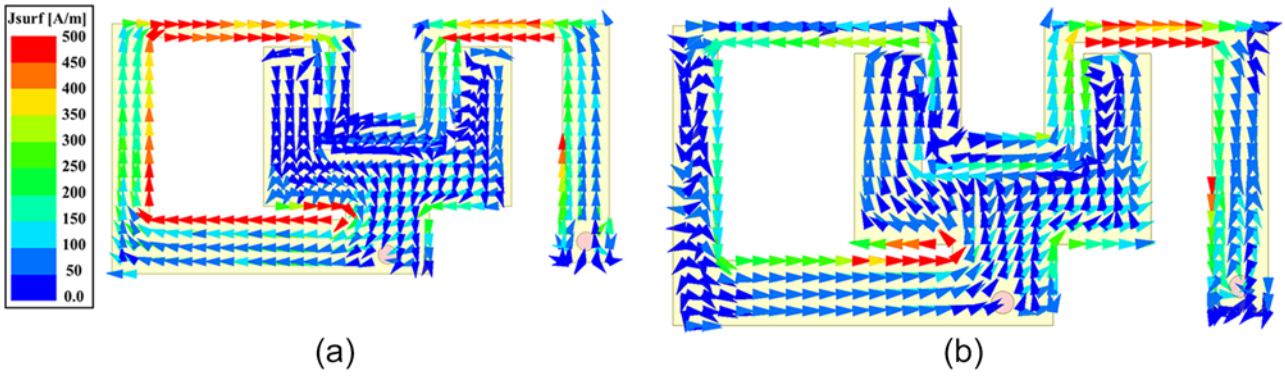

Figure 4. Surface current on the U-shaped feed and open-loop resonator at two resonances of the antenna (a) 3.5 GHz (b) 5.02 GHz.

on both sides of the dual resonances, causing a filtering response to be obtained at both bands, which allows the dual-band MIMO antenna to be susceptible to EM interference at out-of-the-band resonances.

Figure 4 shows the surface current on the U-shaped feed and POLR at two resonances. The maximum current, especially on the left branch of the POLR, is seen at the 1st frequency, whereas the minimal current is found at the 2nd frequency. The current on the

https://doi.org/10.1017/S1759078724001181 Published online by Cambridge University Press

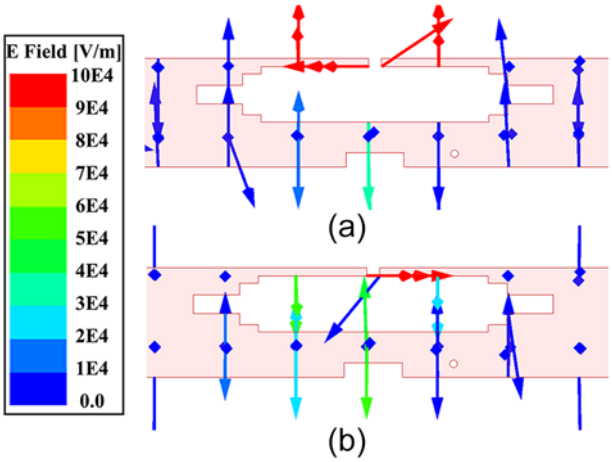

Figure 5. Electric field vector on the open-end staircase slot at two resonances of the antenna (a) 3.5 GHz (b) 5.02 GHz.

POLR exhibits sinusoidal variation over a half cycle, which means the current is maximum at the two ends of the loop resonator with a current null at the centre. The resonant frequency (f_{rL}) of the POLR can be determined using (1)

$$f_{rL} = \frac{c}{2l_{eff}\sqrt{\varepsilon_{eff}}} = \frac{c}{l_{eff}\sqrt{2\,(1+\varepsilon_r)}} \tag{1}$$

Where c is the signal velocity in free space, ε_r is the dielectric constant of the substrate whose value is 4.4 in the designed structure. $\varepsilon_{eff} = (1+\varepsilon_r)/2$ is the effective relative permittivity at the air-dielectric interface [46]. The l_{eff} is the total effective length of the loop resonator, whose approximate value is given as (2)

$$l_{eff} = l_{c1} + 2l_{c3} + l_{c2} + l_{t1} - w_{t1} - g_a \tag{2}$$

At 3.5 GHz, the l_{eff} is equal to 27.85 mm or nearly 0.53 times the guide wavelength. Figure 5 depicts the electric field on the ground plane of the metal side frame at two resonances. Unlike the first frequency, the electric field is found transverse to the OES at the 2nd frequency. For the electric field component $(\bar{E}_z)$ on the OES, the equivalent magnetic current density $(\bar{J}_m)$ can be determined from (3)

$$\bar{J}_m = -\hat{y} \times \bar{E}_z \tag{3}$$

The magnetic current is seen to be longitudinal to the slot length, and its magnitude at two resonances is presented in Fig. 6. The magnetic current density shows that at the 2nd resonance, the OES radiates in the broadside direction along $\pm y$-axis.

Whereas negligible magnetic current is present on the slot at 1st resonance, which means the OES weakly radiates at the 1st resonance frequency.

The physical parameters of OES and POLR can be varied to tune the two operating frequencies independently. Figure 7 reveals the simulated reflection coefficients for different widths (w_d) of POLR and different lengths (l_{s1}) of OES. One can notice that the first resonance shifts toward a higher frequency with an increase in w_d from 0.5–1.3 mm. This can be understood as the increase in the width of the metal strip decreases the inductance of the loop resonator, causing a high-frequency shift of the first resonant frequency. The tuning range of the 1st resonant is achieved over a BW of 320 MHz between 3.22 and 3.54 GHz. It is observed that the change in w_d has a negligible effect on the 2nd resonance. Similarly, the increase in the slot length l_{s1} from 10 to 12 mm lowers the 2nd resonant from

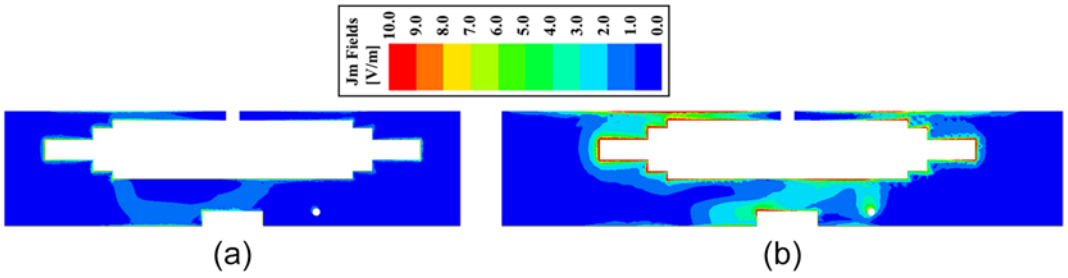

Figure 6. Magnitudes of magnetic current density on the open-end staircase slot at two resonances of the antenna (a) 3.5 GHz (b) 5.02 GHz.

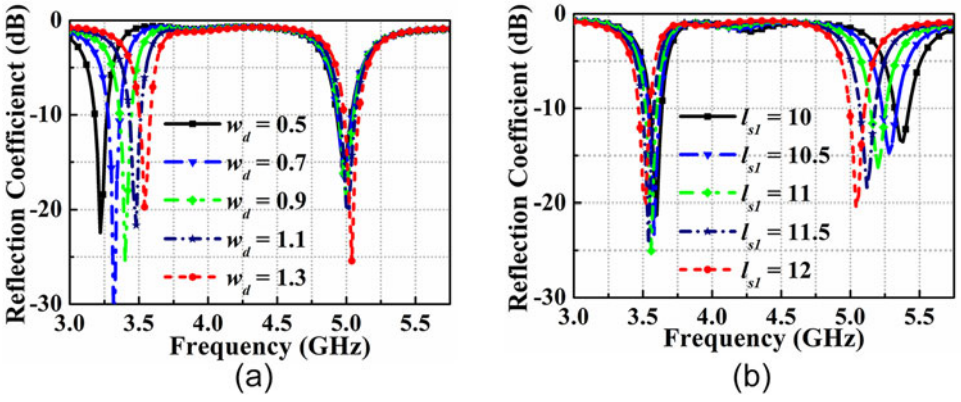

Figure 7. Simulated reflection coefficient of the single MIMO element with change in physical parameters (a) at various widths (w_d) of open-loop resonator (b) at various lengths (l_{s1}) of open-end staircase slot.

https://doi.org/10.1017/S1759078724001181 Published online by Cambridge University Press

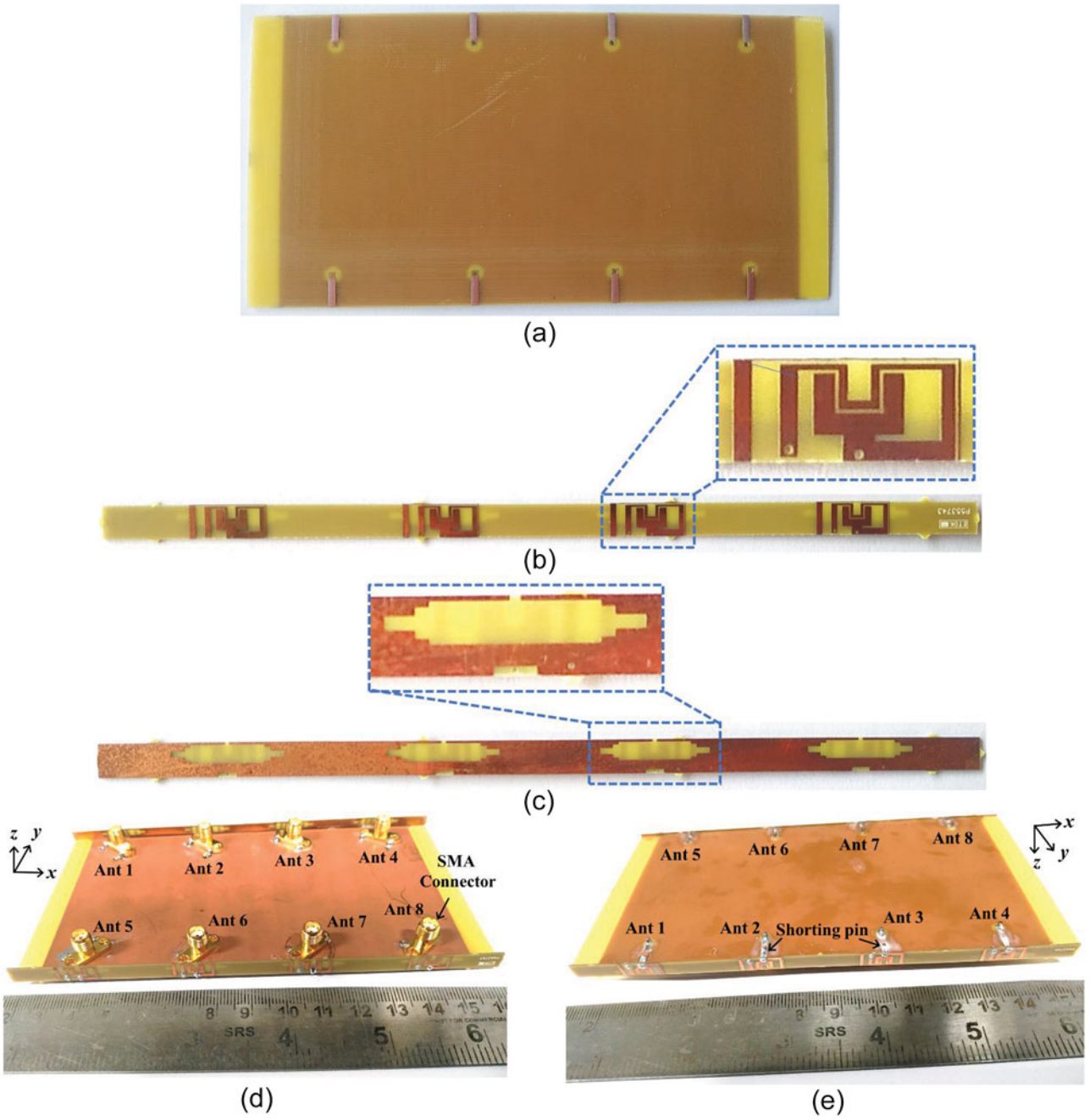

Figure 8. Fabricated photographs of dual-band eight-element MIMO array (a) back layer of SCB consisting of the microstrip feed lines along the long side edges (b) outer face of the narrow metal side frame consisting of POLRs and inverted U-shaped decoupling strips (c) inner face of the narrow metal side frame consisting of staircase OESs. Perspective view of the MIMO array integrated with metal chassis along the edges (d) front-side facing (e) back-side facing.

5.38 to 5.04 GHz with a tuning range of 340 MHz. The increase in l_{s1} enhances the effective current path of the slot mode in the staircase geometry, attributing to the lower frequency shift of the 2nd resonance.

Simulation and measured results of eight-element MIMO

Fabricated MIMO antenna with self-decoupling

Figure 8 shows photographs of the fabricated eight-port dual-band MIMO array, including the back view of the SCB and the front and rear views of the narrow metal side frame. The microstrip feeds and ground plane are engraved on the front and rear faces of a 0.8 mm thick FR-4 substrate. The staircase slots of the MIMO units and POLR-loaded U-shaped feed are patterned on a 0.5 mm thick narrow FR-4 substrate, forming the smartphone's metal frames. These frames are fixed to the SCB using epoxy resin. Isometric views of the final prototype are displayed in Fig. 8(d–e). SMA connectors are soldered to the eight microstrip feed lines, which protrude through the SCB. The U-shaped feed connects to the microstrip line with a 0.2 mm diameter copper wire. Narrow rectangular slits measuring 3.1×0.75 mm^2 are etched on the inner face of the metal frame to isolate the shorting pin from the vertical ground plane. Figure 9 presents the experimental setup of the MIMO array inside

https://doi.org/10.1017/S1759078724001181 Published online by Cambridge University Press

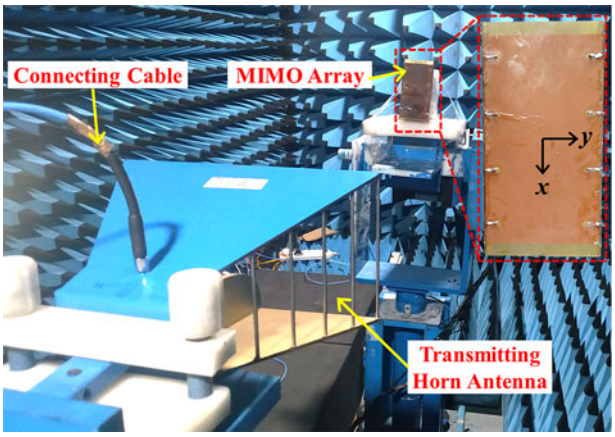

Figure 9. Measurement setup of the dual-band eight-element MIMO array inside an anechoic chamber.

the anechoic chamber, with the distance between the array and the transmitting broadband horn antenna maintained at 100 cm for far-field radiation and gain measurements.

In order to reduce the mutual coupling between antenna units, an inverted U-shaped metal strip is capacitively coupled with the POLR, contributing to the self-decoupling of the MIMO array. Figure 10 illustrates the electric field magnitude on the U-shaped feeding and POLR at the two operating frequencies to gain a physical understanding of the decoupling technique. Here, the antenna on the left side (Ant 4) has been excited, whereas the other antennas of the MIMO array, including Ant 3, are terminated with 50 Ω resistance. Without an inverted U-shaped strip, the notable electric field intensity is detected on the U-shaped feed and POLR of the passive element (Ant 3). Unlike the higher frequency, the coupled field on the passive radiating unit is observed to be significant at the lower frequency, implying low isolation between the two adjacent antennas. This coupling electric field between the units can be remarkably reduced when an inverted U-metal strip is integrated with each antenna structure, causing high isolation between the elements. The improvement in isolation has been achieved because the U-shaped strip acts as a reflector for the surface current, preventing it from coupling with nearby antenna units [47]. Also, due to the nonresonant characteristics of the strip, it provides isolation improvement at both operating frequencies.

Simulated and measured return loss and isolation

The reflection and transmission coefficients of the dual-band MIMO antenna are measured using the Keysigt vector network

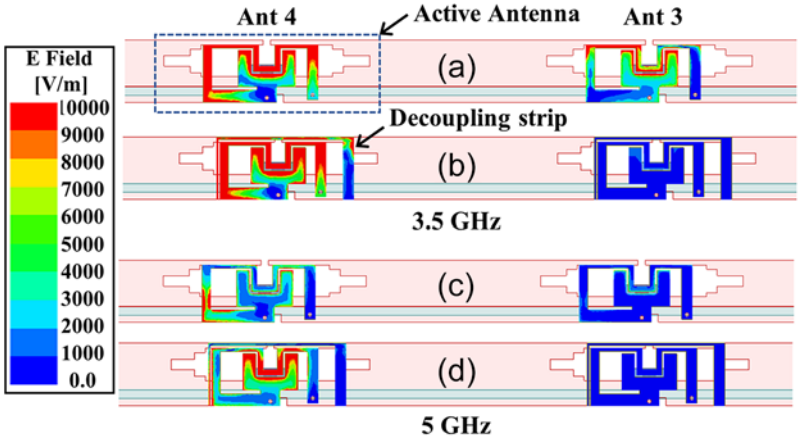

Figure 10. Electric field magnitude on the U-shaped feed and POLR at two operating frequencies of MIMO array (a) and (c) without inverted U-metal strip (b) and (d) with inverted U-metal strip.

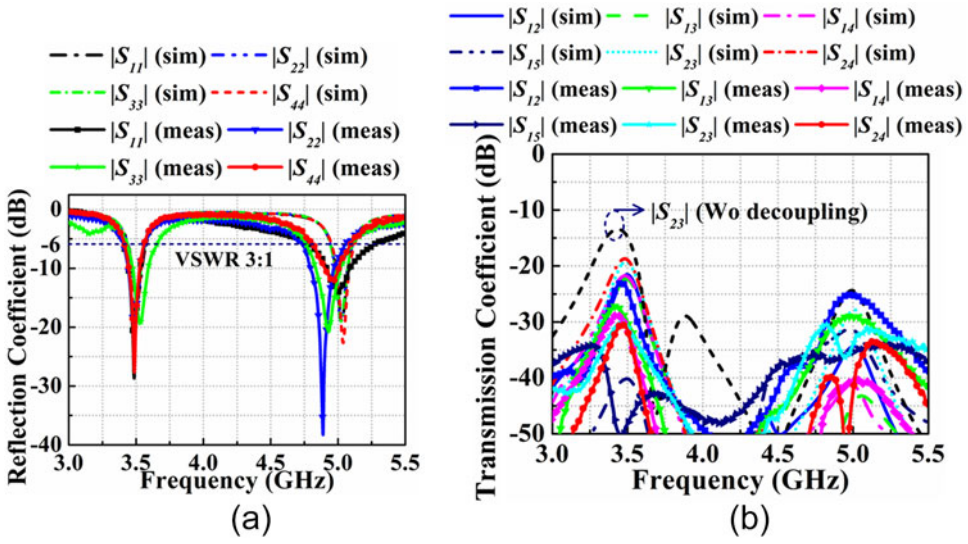

Figure 11. Simulated and measured (a) reflection coefficient (b) transmission coefficient of the dual-band 8 × 8 MIMO array.

https://doi.org/10.1017/S1759078724001181 Published online by Cambridge University Press

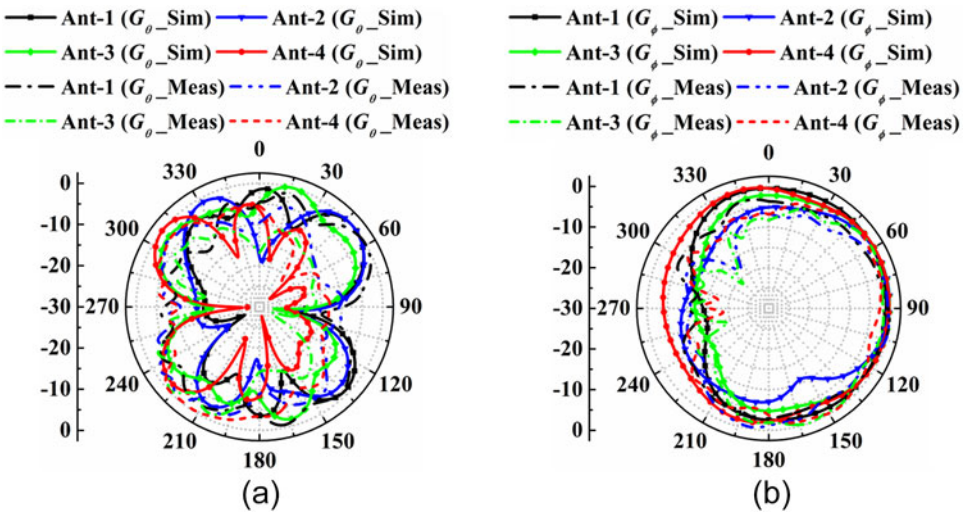

Figure 12. Simulated and measured radiation patterns of the dual-band MIMO array at the lower resonance (a) *xz*-plane (b) *yz*-plane.

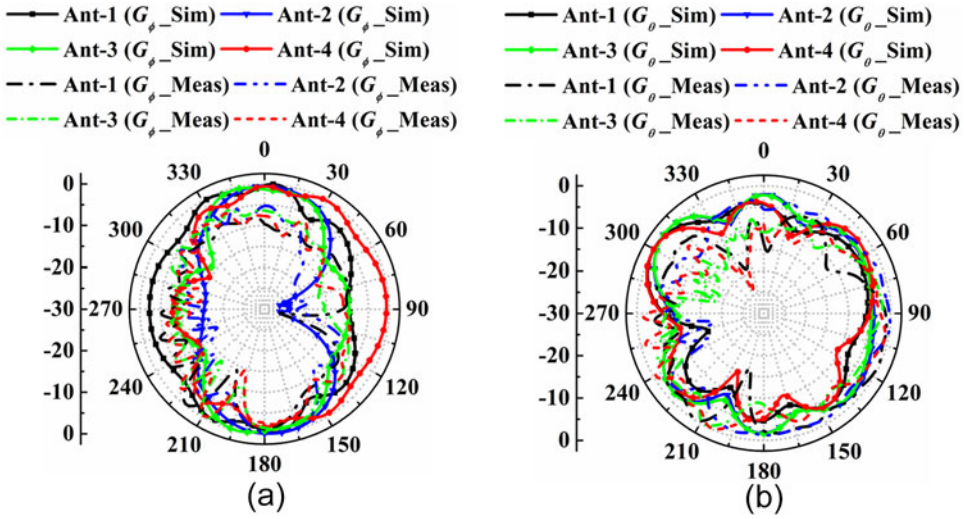

Figure 13. Simulated and measured radiation patterns of the dual-band MIMO array at the higher resonance (a) *xz*-plane (b) *yz*-plane.

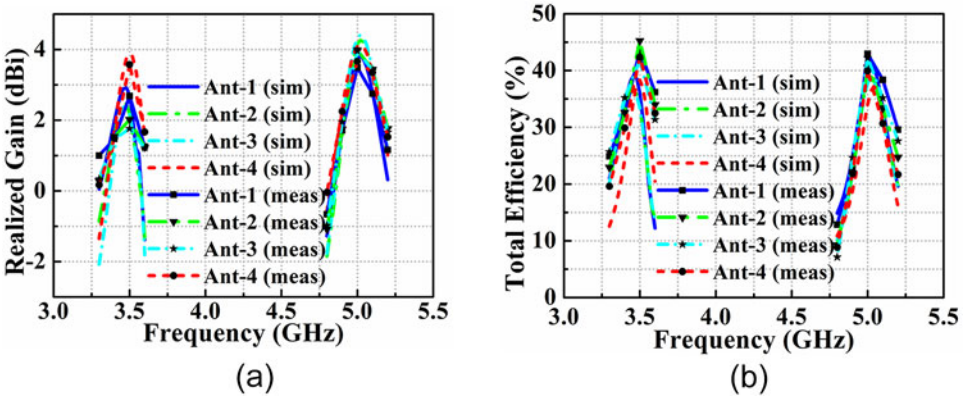

Figure 14. Simulated and measured (a) peak realized gain and (b) total efficiency of the dual-band eight-element MIMO array.

analyzer (VNA) of model PNA N5224B. The simulated and measured reflection coefficients of the eight-port MIMO array are presented in Fig. 11(a). Due to symmetry in the MIMO geometry, only the reflection coefficients of Ant 1 to Ant 4 are presented here. Although the simulated and measured reflection coefficients of the array are found in good agreement, the minor discrepancy

https://doi.org/10.1017/S1759078724001181 Published online by Cambridge University Press

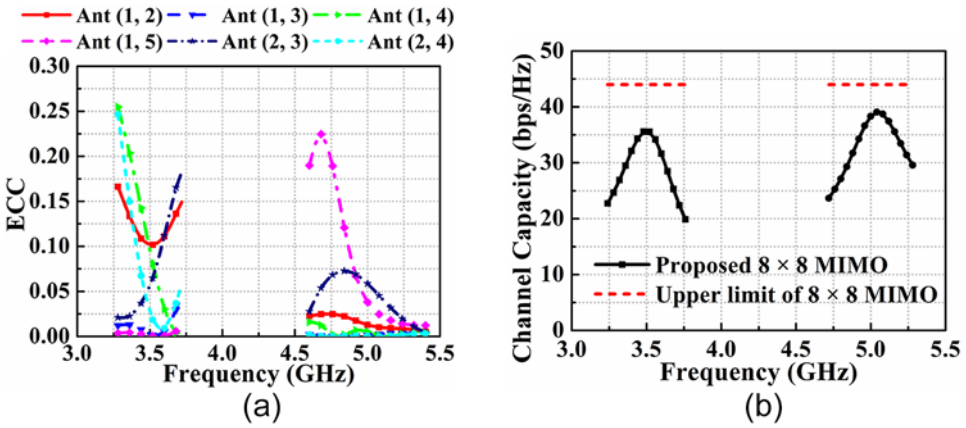

Figure 15. Simulated (a) envelope correlation coefficient (ECC) (b) ergodic channel capacity of the dual-band 8 × 8 MIMO antenna array.

observed may be due to reasons like (a) error introduced during fabrication due to tolerances in minimum metal trace width and spacing between two adjacent traces, (b) effect of small air-gap and epoxy layer that exist between SCB and two metal side-frames along long edges, and (c) minor change in the dielectric constant of FR-4 substrate with temperature and humidity. The designed MIMO exhibits dual resonances at 3.5 and 5.02 GHz in simulation. The return loss that was achieved for Ant 1, Ant 2, Ant 3, and Ant 4 at the lower resonance is found to be 15.9, 16, 15.4, and 20.9 dB; and at the higher resonance, the values are 19.7, 20.8, 20.5, and 17.9 dB. In the measurement, two resonant frequencies are obtained at 3.485 and 5.005 GHz for Ant 1, 3.485 and 4.89 GHz for Ant 2, 3.525 and 4.93 GHz for Ant 3, and 3.485 and 4.97 GHz for Ant 4. The common VSWR 3:1 BW of the MIMO are observed to be over the range of 3.41–3.58 GHz (170 MHz or 4.9%) and 4.94–5.12 GHz (180 MHz or 3.6%) in the simulation. In comparison, the measured response of the MIMO array exhibits the impedance BW between 3.4–3.57 GHz (4.9%) in the lower band and 4.74–5.1 GHz (7.3%) in the higher band. The transmission coefficients (isolation) between the MIMO units are also calculated in full-wave simulation and have been measured using VNA, as revealed in Fig. 11(b). To illustrate the self-decoupling between the elements, the simulated isolation between two nearby antennas without the inverted U-strip is also included. For the self-decoupled array, the simulated minimum isolation between elements is found to be >18.83 dB in the 1st band and >27.68 dB in the 2nd band. As compared to the unloaded strip, the MIMO array exhibits an improvement in isolation of 4.85 and 3.42 dB in the lower and higher resonance, respectively. The measured transmission response of the array exhibits isolation of >22.96 dB in the 1st band and >25 dB in the 2nd band, respectively.

Radiation patterns, gain and total efficiency

The radiation pattern of the proposed dual-band MIMO array was measured for the unit elements Ant 1, Ant 2, Ant 3, and Ant 4. The radiation pattern was measured in two principal planes (*xz* and *yz*), for which only one of the elements has been excited, and the remaining ports of the array are terminated with a broadband 50 Ω load impedance. Figures 12 and 13 display the 2D polar radiation patterns of the MIMO array in the two orthogonal planes (*xz* and *yz*) at the two resonances near 3.5 and 5 GHz. The measured radiation patterns are found to be consistent with those of the simulated

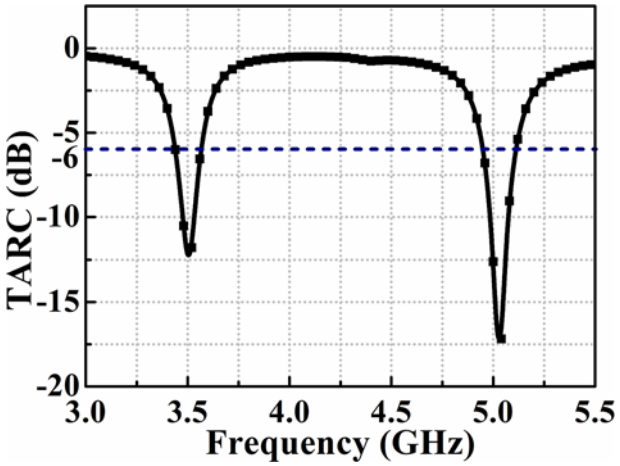

Figure 16. Simulated total active reflection coefficient (TARC) of the MIMO array.

response, except for a minor disagreement in the *xz*-plane. This discrepancy may arise due to errors revealed in the measurement setup inside the anechoic chamber or due to the presence of an air gap and misalignment between the metal side frame and the SCB. In the *xz*-plane, the pattern shows bi-directional radiation in the shape of a figure of eight, whereas, in the yz-plane, the pattern is found to be in the endfire direction outward to the staircase OES. It can also be concluded from Figs. 12 and 13 that the polarization of the MIMO element at the two operating frequencies appears to be dual-orthogonal linearly polarized. The simulated and measured gain and total efficiency of the MIMO array are depicted in Fig. 14(a–b). At the lower frequency, the peak realized gain of Ant 1 to Ant 4 are 2.91, 2.49, 2.39, and 3.9 dBi in simulation against the measured values of 2.68, 2, 1.76, and 3.57 dBi. Whereas at the higher operating frequency, the simulated gains of Ant 1 to Ant 4 are 3.81, 4.26, 4.42, and 4.14 dBi, respectively and that of 3.48, 3.98, 3.9, 3.67 dBi as found in the measurement. At the 1st and 2nd operating frequencies, the simulated maximum total efficiencies of the array are 37.98% and 40.2%. The measured efficiency of the array is determined using the Wheeler cap method as given in [16]. The efficiencies of Ant 1 to Ant 4 are calculated as 43.6%, 45.3%, 41.8%, and 42.4% near 3.5 GHz and 42.9%, 40.5%, 42.2%, and 39.9% near 5 GHz. The slightly lower efficiency as compared to earlier reported dual-band MIMO array is attributed to the higher dielectric losses

https://doi.org/10.1017/S1759078724001181 Published online by Cambridge University Press

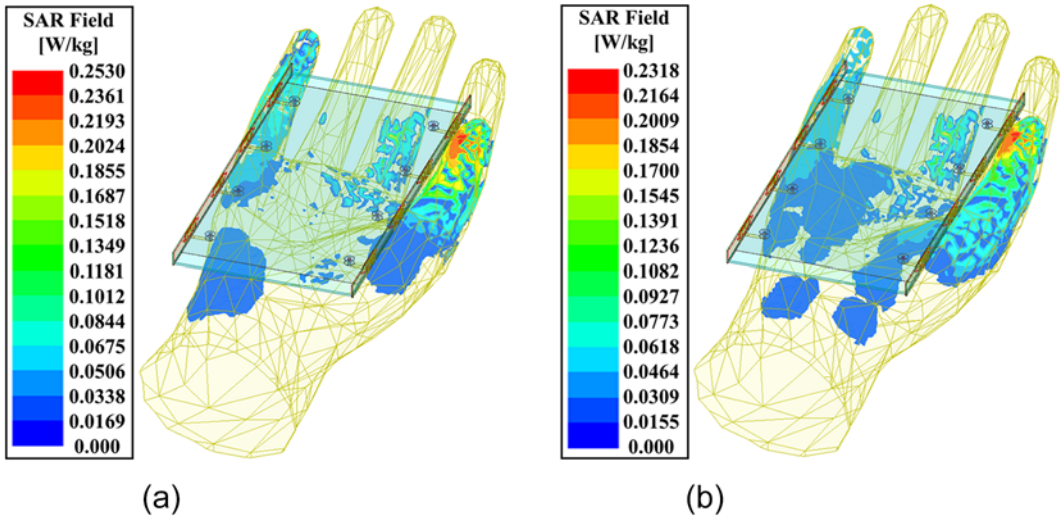

Figure 17. Simulated SAR distribution on user's hand for SHM operation (a) 3.5 GHz (b) 5 GHz.

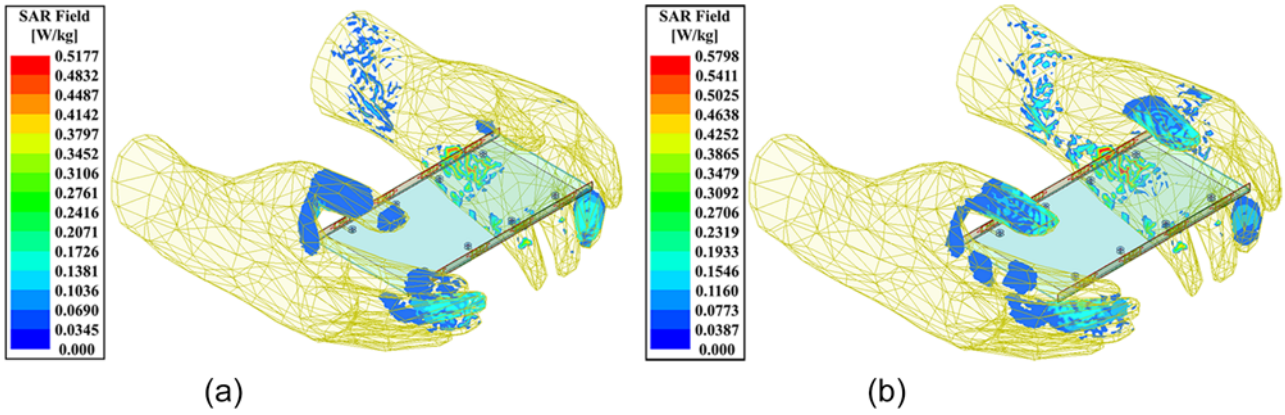

Figure 18. Simulated SAR distribution on user's hand for DHM operation (a) 3.5 GHz (b) 5 GHz.

of the FR-4 substrate. It can be shown that for the loss-less substrate of metal side-frames, peak efficiencies of Ant 1, Ant 2, Ant 3, and Ant 4 reach 50.8%, 46.9%, 44.7%, and 63.9% at the lower frequency and that of 60.9%, 61%, 60.9%, and 64.1% at the higher frequency.

Diversity parameters and SAR analysis

Envelope correlation coefficient and CC

The diversity and multiplexing analysis of the dual-band MIMO array focuses on evaluating the envelope correlation coefficient (ECC) and ergodic CC. Figure 15 depicts the ECC and CC of the eight-element MIMO array. The ECC quantifies the correlation between individual antenna elements, with lower values indicating higher diversity gain (DG), which is advantageous in MIMO systems. It is crucial to ensure ECC values remain below certain thresholds for optimal system operation. The ECC between two antennas is calculated using the complex radiation far-field patterns, as shown in (4) [38]

$$ECC = \rho_{ij}^2 = \frac{\left|\oint\oint \bar{F}_i(\theta,\varphi).\bar{F}_j(\theta,\varphi)\sin\theta d\theta d\varphi\right|^2}{\oint\oint\left|\bar{F}_i(\theta,\varphi)\right|^2\sin\theta d\theta d\varphi \oint\oint\left|\bar{F}_j(\theta,\varphi)\right|^2\sin\theta d\theta d\varphi} \quad (4)$$

Table 2. Material properties of the smartphone model

Part	Material	Electrical property
Battery cell	Copper	Cond. = 5.8×10^7 S/m
Front and rear covers	HDPE plastic	$\epsilon_r = 2.3$, $tan\ \delta = 0.0005$
LCD panel, camera	Glass	$\epsilon_r = 4.82$, $tan\ \delta = 0.0054$

In the above equation, ECC is considered as the square of the correlation coefficient (ρ_{ij}). Here $\overline{F_j}(\theta,\phi)$ in (4) signifies the radiated electric field. Considering coupling between all the ports of the designed dual-band MIMO antenna, the simulated ECC has a maximum value of <0.174 in the lower band and <0.069 in the higher band (see Fig. 15[a]). The obtained value is below the limit of 0.3 for the MIMO diversity operation in the sub-6 GHz 5G range. Within the two operating bands, the DG of the suggested MIMO antenna was found above 9.85 and 9.98, as determined using $DG = 10\sqrt{1 - ECC^2}$.

The CC, representing the maximum achievable data transmission rate, is determined by considering system parameters such as signal-to-noise ratio (SNR), antenna efficiency, and environmental conditions. For the designed dual-band 8 × 8 MIMO antenna, the

https://doi.org/10.1017/S1759078724001181 Published online by Cambridge University Press

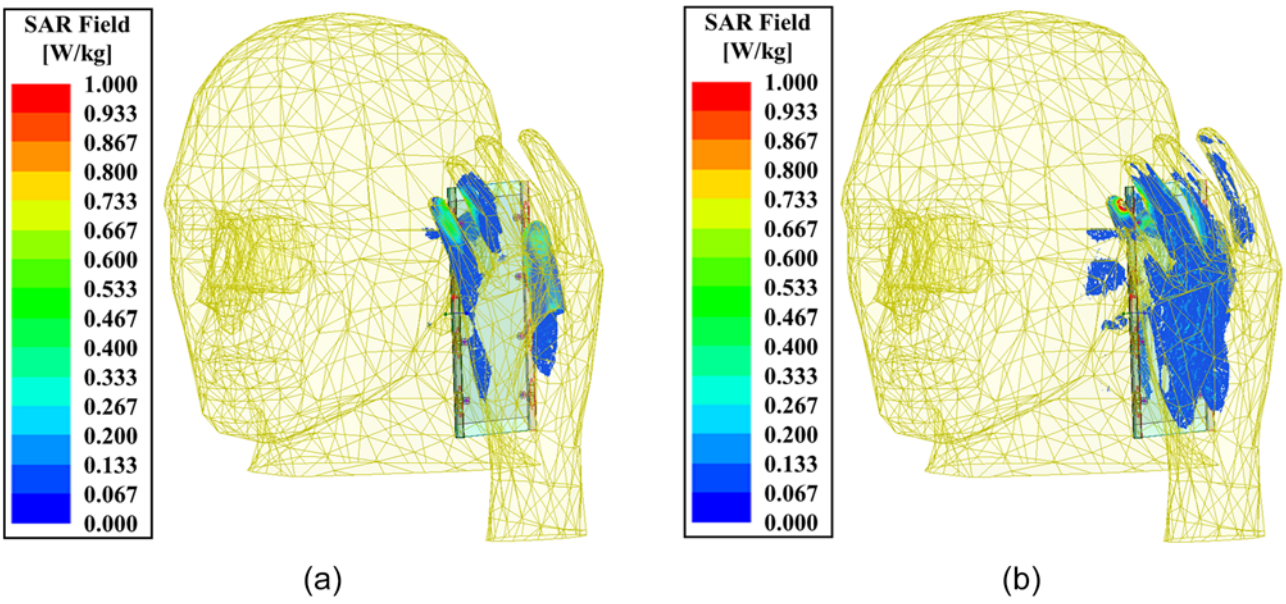

Figure 19. Simulated SAR distribution on the human hand and head phantom models for calling mode (a) 3.5 GHz (b) 5 GHz.

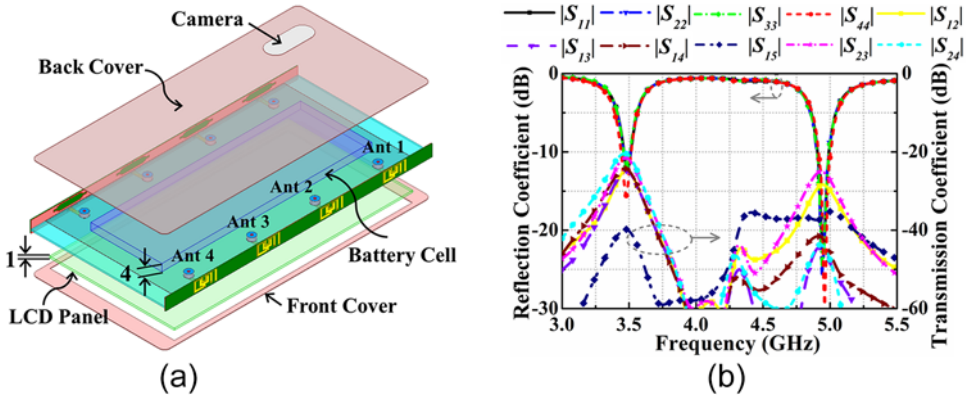

Figure 20. (a) Smartphone model of the proposed dual-band eight-element MIMO antenna (b) simulated reflection and transmission coefficients including the effect of battery, LCD screen, front and rear covers.

Kronecker model has been employed to determine ergodic CC as given by (5) [38]

$$CC = \log_2\left[\det\left(I + \frac{SNR}{N_T} H_c * {H_c}^T\right)\right] \quad (5)$$

In the above relation, $\boldsymbol{I}$ is an $N_T \times N_T$ identity matrix, where N_T is the number of antennas in the transmitter (Tx). The SNR is the signal-to-noise ratio at the receiver (Rx). The channel is considered independent identically distributed (iid) complex Gaussian variables with zero mean and unit variance. All the antennas in the Tx terminal are assumed to be uncorrelated and have 100% efficiency. The channel matrix (H_c) can be calculated from the correlation coefficient (ρ_{RX}) and total efficiency (η_{RX}) of the receiving MIMO antennas using (6)

$$H_c = \sqrt{\rho_{scale,RX}} H_{iid}, \text{ with } \rho_{scale,RX} = \sqrt{\eta_{RX}} \rho_{RX} \sqrt{\eta_{RX}} \quad (6)$$

Here H_{iid} is the complex random variable. One should notice that the operator $(.)^T$ is the Hermitian transpose of the channel matrix. The CC obtained using (5) and (6) is averaged over 10000 arbitrary Rayleigh fading conditions. The simulated CC of the eight-port dual-band MIMO array is given in Fig. 15(b) and compared with that of an ideal 8 × 8 MIMO antenna for a fixed SNR value of 20 dB. The designed array exhibits a maximum CC of 35.5 and 39.1 bps/Hz in the two operating frequencies, which is very close to the theoretical upper limit of 44 bps/Hz for the eight-element MIMO antenna.

In multipath fading, the incoming signals at the different ports of the dual-band MIMO antenna face random phase variation. The signal at one port will couple to the other ports due to mutual coupling and can affect the impedance matching of the MIMO elements. The total active reflection coefficient (TARC) is the matric that correctly characterizes the BW of the MIMO array in the presence of inter-port coupling and is defined as the square root of the total reflected power to the total incident power. For N-port MIMO antenna TARC is given by (7) [48].

$$TARC = N^{-0.5} \sqrt{\sum_{i=1}^{N} \left| \sum_{k=1}^{N} |S_{ik}| \exp\left[j\left(\angle S_{ik} + \theta_{k-1}\right)\right] \right|^2} \quad (7)$$

Where $S_{ik} = |S_{ik}| \angle S_{ik}$ is the complex scattering parameter for the 8 × 8 MIMO array. The incident wave on each port has a random

https://doi.org/10.1017/S1759078724001181 Published online by Cambridge University Press

https://doi.org/10.1017/S1759078724001181 Published online by Cambridge University Press

Table 3. State-of-the-art performance comparison of the dual-band eight-port MIMO array with earlier reported works

Ref.	Freq. (GHz)	AP	Impedance BW	Multiband technique	Isolation (dB)	Decoupling method	Efficiency	ECC	Peak CC (bps/Hz)	Slot/Antenna size (mm^2)	MIMO order	Metal-side frame
[26]	3.5	Yes	3.33–3.67 GHz (9.7%)	NA	>17	Pattern diversity	52–65%	<0.16	NR	25 × 3.5	8 × 8	No
[27]	3.55	Yes	3.5–3.6 GHz (2.8%)	NA	>15	Pattern diversity	44–53%	<0.15	36	44.7 × 14.9	8 × 8	No
[29]	3.5	No	3.33–3.67 (9.7%)	NA	>19.1	Self-isolation	60%	<0.0125	34	17.4 × 6	8 × 8	Yes
[30]	3.53	No	3.39–3.67 GHz (7.93%)	NA	>17.5	Pol. diversity & reduced ground effect	62–76%	<0.05	40.8	20.5 × 3	8 × 8	No
[31]	3.5	Yes	3.4–3.6 GHz (5.7%)	NA	>17	Self-isolation using I-shaped strip	58%	<0.1	19	20 × 7	4 × 4	Yes
[32]	3.5	No	3.4–3.6 GHz (5.7%)	NA	>10	Self-isolation	65–78%	<0.055	54.3	6 × 6.5	10 × 10	Yes
[35]	1.84, 3.5	No	1.8–1.88 (4.3%) 3.4–3.6 (5.7%)	Inverted F-antenna	>15, >18	Composite lumped capacitor	62–66%, 50–62%	<0.046, <0.064	NR	10 × 23.1	2 × 2	No
[36]	3.62, 5.6	No	3.4–3.84 GHz (12.2%) 5.15–6.05 GHz (16.1%)	Inverted π-strip, longer & shorter open-end slots)	>12, >12.5	Spatial diversity	41–82%, 47–79%	<0.15, <0.1	37, 29.5	15 × 7 10.5 × 3 7 × 2.5	8 × 8, 6 × 6	No
[37]	3.6, 5.51	No	3.4–3.8 GHz (11.1%) 5.1–5.925 GHz (14.9%)	T-shaped slot	>11, >11.5	Self-isolation	42–65% 62–82%	<0.15, <0.05	48, 51.4	16.2 × 3	10 × 10	No
[38]	3.5, 5.53	No	3.4–3.6 GHz (5.7%) 5.15–5.925 GHz (14%)	L-shaped slot in SIR configuration	>11.2	Self-isolation	51–59% 62–80%	<0.08	36.9	9.6 × 15.2	8 × 8	No
[39]	2.55, 3.45	No	2.4–2.7 GHz (11.8%) 3.3–3.6 GHz (8.7%)	Folded monopole	>15.1	Grounded branch	65–80%* 61–78%*	<0.21	35	6.8 × 4	8 × 8	Yes
[40]	3.5, 4.9	Yes	3.4–3.6 GHz (5.7%) 4.8–5 GHz (5.7%)	Capacitive coupled U-shaped strips	>17.5, >20	Self-isolation using I-shaped strip	52–65%, 50–79%	<0.14, <0.12	18.3	22 × 7	4 × 4	Yes
[41]	3.5, 4.9	No	3.1–3.85 GHz (21.6%) 4.8–6 GHz (22.2%)	Folded monopole	>17, >15	Polarization diversity + neutralization line	65–75%, 60–71%	<0.06	39.5,	17.85 × 5	8 × 8	Yes
[42]	3.5, 4.95	No	3.4–3.6 GHz (5.7%) 4.8–5.1 GHz (6.1%)	Folded monopole & coupled loop branch	>11.5, >13	Neutralization line	41–72%, 40–85%	<0.08, <0.05	38.5, 38	15 × 7	8 × 8	Yes

(*Continued*)

Table 3. (*Continued.*)

Ref.	Freq. (GHz)	AP	Impedance BW	Multiband technique	Isolation (dB)	Decoupling method	Efficiency	ECC	Peak CC (bps/Hz)	Slot/Antenna size (mm^2)	MIMO order	Metal-side frame
[43]	3.49, 5.54	No	3.27–3.72 GHz (12.9%) 5–6.08 GHz (19.5%)	U-shape monopole and L-shape OES	>15, >12	Self-isolation	50–56%, 53–65%	<0.1, <0.04	38.8, 39.7	14.9 × 5.2	8 × 8	Yes
[45]	3.55, 5.36	No	3.3–3.8 GHz (14.1%) 4.8–5.925 GHz (20.9%)	OES and coupled fed & parasitic arms	>10.5	Self-isolation	55–72%, 43–73%	<0.12	36.8, 37.6	15 × 3	8 × 8	Yes
This work	3.48, 4.92	No	3.4–3.57 GHz (4.9%) 4.74–5.1 GHz (7.3%)	Staircase OES and POLR	>22.96, >25	Self-isolation using inverted U-strip	37.98%, 40.2%	<0.174, <0.069	35.5, 39.1	18.6 × 5.8	8 × 8	Yes

[#]SIR = stepped impedance resonator, CC = channel capacity.
*Radiation efficiency, AP = antenna pair, OES = open-end slot, POLR = parasitic open-loop resonator, NR = not reported, NA = not applicable.

phase of "θ_k" whose value can be between 0 and 2π. Note that the reference phase (θ_0) at port-1 is considered zero. Figure 16 depicts the simulated TARC of the dual-band MIMO antenna, exhibiting a reflection coefficient of below −6 dB over the operating range of 3.41–3.58 GHz and 4.94–5.12 GHz.

SAR analysis

SAR is an absorbed EM power by the unit mass of the body tissue when it is exposed to radiation and it is represented in the unit of W/kg or mW/g. For mobile operation at microwave frequency, the maximum allowable limits of SAR on the human body are 1.6 and 2 W/kg when the averaging of electric field intensity is performed over 1 and 10 gm of tissue, respectively. Figures 17 and 18 reveal the average SAR on the human hand for two popular cases of single-hand mode (SHM) and dual-hand mode (DHM) at the two center frequencies. These two modes are related to the mobile operations, e.g. internet browsing and online video gaming. All eight elements of the MIMO array were excited with a power of 10 dBm each. The SAR on the human hand is found to be well below the acceptable limit. At 3.5 and 5 GHz, the peak SAR values are 0.253 and 0.232 W/kg for SHM; on the contrary, the values are 0.518 and 0.579 W/kg for DHM. The effect of microwave radiation on the human head is analyzed during calling mode for an input power of 10 dBm per unit element of the array. The SAR on the human head model is shown in Fig. 19 at two frequencies, 3.5 and 5 GHz. At the lower band, the SAR is obtained <0.667 W/kg within the major area of the hand and head phantom, whereas it is <0.2 W/kg for the higher band. It is noteworthy that, despite the reflection of waves from the human body tissue, the impedance matching of the antenna units remains well below −10 dB for SHM and DHM operations.

Effect of battery and LCD display

The effect of the battery, LCD screen, and front and back covers on the reflection coefficient and transmission coefficient response of the array has been investigated. The battery having a cuboidal size of 118 × 40 × 4 mm^3 is placed on the side of the system ground plane. The material for the battery is considered copper, which has a conductivity of 5.8×10^7 S/m. On the contrary the LCD panel of thickness 1 mm is placed on the opposite side of the battery, which covers a lateral size of 134 × 70 mm^2. To account for the encapsulation inside the smartphone, the dual-band MIMO antenna is covered by front and rear covers of plastic material. Figure 20(a) presents the schematic of the eight-element MIMO array covered by different parts of the smartphone. Material properties of the various parts are listed in Table 2, which shows that the LCD and camera lens are made of glass material, and the front and back covers of the phone are made of High-Density Polyethylene (HDPE) plastic material [49]. Figure 20(b) shows the simulated reflection and transmission coefficients of the MIMO array, considering the effects of smartphone casing, battery and LCD screen. The impedance matching of the array slightly deteriorates at the lower resonance, with a minimum value of return loss achieved as 11.82 dB for Ant 3. The MIMO antenna exhibits a slightly better transmission coefficient response with isolation between adjacent units is >20.37 dB in the lower band, and it is >24.98 dB in the higher band.

Table 3 represents the performance comparison of the designed MIMO antenna with earlier reported single and dual-band massive MIMO arrays. The salient feature of the present work is obtaining high isolation simultaneously at the two operating frequencies by integrating the decoupling circuit with antenna geometry. The isolation between the adjacent units of the proposed dual-band MIMO antenna is achieved to be better than all the similar works listed in Table 3. Although MIMO arrays in references [39–41] exhibit low mutual coupling between the elements, but additional coupling reduction circuit is placed between the radiating units. The ground branch in reference [39] occupies a large area of the SCB, making it unlikely to be used in a practical scenario. Also, the CC of reference [40] is much lower compared to the proposed work, which is due to the implementation of a lower MIMO order; apart from that, the element's size of the array is also higher than the suggested dual-band radiating unit.

Conclusion

A new dual-band eight-port MIMO antenna with high isolation characteristics has been designed for future 5G smartphone applications. The unit element of the MIMO array is chosen as a coupled resonating element in the geometry of a staircase OES and a loop branch meandered around a U-shaped feed. The multi-resonance characteristics of the unit element have been showcased by analyzing the surface current on the structure. The designed antenna's features, like independent frequency tuning of the two operating bands, were detailed by the change in the physical parameters of the slot and POLR. The proposed dual-band MIMO array resonates near 3.5 and 5 GHz with impedance BWs of 170 and 360 MHz, respectively. For the massive 8 × 8 MIMO geometry, the decoupling between adjacent units was obtained by combining the inverted U-shaped strip with each antenna element without the requirement of any additional space in the SCB or in the metal side frames. The recommended array demonstrates high isolation of over 22 dB simultaneously at the two center frequencies, with a minimum improvement of 3.42 dB observed in reversing the coupling compared to the reference MIMO array. To the best of the authors' knowledge, this low mutual coupling is found to be better as compared to all the reported dual-band MIMO antennas of an element size of 8 or more. The proposed MIMO antenna array also exhibits low SAR values at different operating modes, demonstrating its potential application in the future 5G mobile terminal. The efficiency and BW of the dual-band MIMO array can be further improved by implementing the narrow side frames on substrates of lower dielectric constant and loss tangent.

Acknowledgements. One of the authors appreciates the support received from the Department of Science and Technology, Govt. of India and also acknowledges the IEEE Antennas and Propagation Society for the 2023 APSF fellowship. This work is supported by the Science and Engineering Research Board (SERB), Government of India, under Project no. TTR/2022/000001.

Competing interests. The authors report no conflict of interest.

References

1. **Nam Y-H, Ng BL, Sayana K, Li Y, Zhang J, Kim Y, Lee J** (2013) Full-dimension MIMO (FD-MIMO) for next generation cellular technology. *IEEE Communications Magazine* **51**(6), 172–179.
2. **Hussain R, Alreshaid AT, Podilchak SK and Sharawi MS** (2017) Compact 4G mimo antenna integrated with a 5G array for current and future mobile handsets. *IET Microwaves, Antennas & Propagation* **11**(2), 271–279.

https://doi.org/10.1017/S1759078724001181 Published online by Cambridge University Press

3. **Roslan SF, Kamarudin MR, Khalily M and Jamaluddin MH** (2014) An MIMO rectangular dielectric resonator antenna for 4G applications. *IEEE Antennas and Wireless Propagation Letters* **13**, 321–324.
4. **Jha KR and Sharma SK** (2018) Combination of MIMO antennas for handheld devices [wireless corner]. *IEEE Antennas and Propagation Magazine* **60**(1), 118–131.
5. **Sharawi MS, Numan AB, Khan MU and Aloi DN** (2012) A dual-element dual-band MIMO antenna system with enhanced isolation for mobile terminals. *IEEE Antennas and Wireless Propagation Letters* **11**, 1006–1009.
6. **Kumar S, Dixit AS, Malekar RR, Raut HD and Shevada LK** (2020) Fifth generation antennas: A comprehensive review of design and performance enhancement techniques. *IEEE Access* **8**, 163568–163593.
7. **Hong W, Jiang ZH, Yu C, Hou D, Wang H, Guo C, Hu Y, Kuai L, Yu Y, Jiang Z and Chen Z** (2021) The role of millimeter-wave technologies in 5G/6G wireless communications. *IEEE Journal of Microwaves* **1**(1), 101–122.
8. **Wang C, Li E and Sievenpiper DF** (2017) Surface-wave coupling and antenna properties in two dimensions. *IEEE Transactions on Antennas and Propagation* **65**(10), 5052–5060.
9. **Deng H and Zhu L** (2023) Systematic design method for mutual coupling reduction in closely spaced patch antennas. *IEEE Open Journal of Antennas and Propagation* **4**, 349–360.
10. **Yang X, Liu Y, Xu Y-X and Gong S-X** (2017) Isolation enhancement in patch antenna array with fractal UC-EBG structure and cross slot. *IEEE Antennas and Wireless Propagation Letters* **16**, 2175–2178.
11. **Alibakhshikenari M, Khalily M, Virdee BS, See CH, Abd-Alhameed RA and Limiti E** (2019) Mutual-coupling isolation using embedded metamaterial EM bandgap decoupling slab for densely packed array antennas. *IEEE Access* **7**, 51827–51840.
12. **Dash JC and Sarkar D** (2022) A four-port CSRR-loaded dual-band MIMO antenna with suppressed higher order modes. *IEEE Access* **10**, 30770–30778.
13. **Ayatollahi M, Rao Q and Wang D** (2012) A compact, high isolation and wide bandwidth antenna array for long term evolution wireless devices. *IEEE Transactions on Antennas and Propagation* **60**(10), 4960–4963.
14. **Chen Y-S and Chang C-P** (2016) Design of a four-element multiple-input–multiple-output antenna for compact long-term evolution small-cell base stations. *IET Microwaves, Antennas & Propagation* **10**(4), 385–392.
15. **Al-Hasan M, Ben Mabrouk I, Almajali ERF, Nedil M and Denidni TA** (2019) Hybrid isolator for mutual-coupling reduction in millimeter-wave MIMO antenna systems. *IEEE Access* **7**, 58466–58474.
16. **Dey S and Koul SK** (2021) Isolation improvement of MIMO antenna using novel EBG and hair-pin shaped DGS at 5G millimeter wave band. *IEEE Access* **9**, 162820–162834.
17. **Islam H, Das S, Ali T, Bose T, Kumari S, Prakash O and Kumar P** (2022) Bandstop filter decoupling technique for miniaturized reconfigurable MIMO antenna. *IEEE Access* **10**, 19060–19071.
18. **Garg P and Jain P** (2020) Isolation improvement of MIMO antenna using a novel flower shaped metamaterial absorber at 5.5 GHz WiMAX band. *IEEE Transactions on Circuits and Systems II: Express Briefs* **67**(4), 675–679.
19. **Dey S, Sarma D and Dey S** (2024) A miniaturized frequency selective dual band metamaterial absorber for mutual coupling reduction between microstrip Antennas. In *IEEE Wireless Antenna and Microwave Symposium (WAMS)*, Visakhapatnam, India, pp. 1–5.
20. **Dey S, Keerthi MS and Dey S** (2023) Broadband millimeter wave MIMO antennas at 28 GHz with low mutual coupling using frequency selective surface wall. In *IEEE Microwaves, Antennas, and Propagation Conference (MAPCON)*, IEEE, Ahmedabad, India, 1–6.
21. **Li M, Jiang L and Yeung KL** (2020) A general and systematic method to design neutralization lines for isolation enhancement in MIMO antenna arrays. *IEEE Transactions on Vehicular Technology* **69**(6), 6242–6253.
22. **Li M and Cheung S** (2021) A novel calculation-based parasitic decoupling technique for increasing isolation in multiple-element MIMO antenna arrays. *IEEE Transactions on Vehicular Technology* **70**(1), 446–458.
23. **Wu C-H, Chiu C-L and Ma T-G** (2016) Very compact fully lumped decoupling network for a coupled two-element array. *IEEE Antennas and Wireless Propagation Letters* **15**, 158–161.
24. **Hu H-T, Chen F-C and Chu Q-X** (2016) A compact directional slot antenna and its application in MIMO array. *IEEE Transactions on Antennas and Propagation* **64**(12), 5513–5517.
25. **Sharma Y, Sarkar D, Saurav K and Srivastava KV** (2017) Three-element MIMO antenna system with pattern and polarization diversity for WLAN applications. *IEEE Antennas and Wireless Propagation Letters* **16**, 1163–1166.
26. **Xu Z and Deng C** (2020) High-isolated MIMO antenna design based on pattern diversity for 5G mobile terminals. *IEEE Antennas and Wireless Propagation Letters* **19**(3), 467–471.
27. **Ding CF, Zhang XY, Xue C-D and Sim C-Y-D** (2018) Novel pattern-diversity-based decoupling method and its application to multielement MIMO antenna. *IEEE Transactions on Antennas and Propagation* **66**(10), 4976–4985.
28. **Dey S, Vel KS, Asok AO and Dey S** (2022) Novel self isolated multiple input and multiple output antenna using pattern diversity method for 5.5 GHz WiMAX application. In *Asia-Pacific Microw. Conf. (APMC)*, Yokohama, Japan, 399–401.
29. **Zhao A and Ren Z** (2019) Size reduction of self-isolated MIMO antenna system for 5G mobile phone applications. *IEEE Antennas and Wireless Propagation Letters* **18**(1), 152–156.
30. **Li Y, Sim C-Y-D, Luo Y and Yang G** (2019) High-isolation 3.5 GHz eight-antenna MIMO array using balanced open-slot antenna element for 5G smartphones. *IEEE Transactions on Antennas and Propagation* **67**(6), 3820–3830.
31. **Ren Z, Zhao A and Wu S** (2019) MIMO antenna with compact decoupled antenna pairs for 5G mobile terminals. *IEEE Antennas and Wireless Propagation Letters* **18**(7), 1367–1371.
32. **Alja'afreh SS, Altarawneh B, Alshamaileh MH, E'qab RA, Hussain R, Sharawi MS, Xing L and Xu Q** (2021) Ten antenna array using a small footprint capacitive-coupled-shorted loop antenna for 3.5 GHz 5G smartphone applications. *IEEE Access* **9**, 33796–33810.
33. **Sui J and Huang C** (2022) Multi-element fully decoupled inverted-F antennas for mobile terminals. *IEEE Transactions on Antennas and Propagation* **70**(11), 10076–10085.
34. **Sui J, Dou Y and Mei X** (2020) Self-curing decoupling technique for MIMO antenna arrays in mobile terminals. *IEEE Transactions on Antennas and Propagation* **68**(2), 838–849.
35. **Sui J, Cheng Y-F, Fang X, Li D, Zhu X and Yuan X** (2024) A dual-band decoupling technique for MIMO antenna systems using composite capacitor circuits. *IEEE Transactions on Circuits and Systems II: Express Briefs* **71**(1), 116–120.
36. **Li Y, Sim C-Y-D, Luo Y and Yang G** (2018) 12-port 5G massive MIMO antenna array in sub-6GHz mobile handset for LTE bands 42/43/46 applications. *IEEE Access* **6**, 344–354.
37. **Li Y, Sim C-Y-D, Luo Y and Yang G** (2018) Multiband 10-antenna array for sub-6 GHz MIMO applications in 5-G smartphones. *IEEE Access* **6**, 28041–28053.
38. **Li J *et al.*** (2019) Dual-band eight-antenna array design for MIMO applications in 5G mobile terminals. *IEEE Access* **7**, 71636–71644.
39. **Jiang W, Cui Y, Liu B, Hu W and Xi Y** (2019) A dual-band MIMO antenna with enhanced isolation for 5G smartphone applications. *IEEE Access* **7**, 112554–112563.
40. **Ren Z and Zhao A** (2019) Dual-band MIMO antenna with compact self-decoupled antenna pairs for 5G mobile applications. *IEEE Access* **7**, 82288–82296.
41. **Serghiou D, Khalily M, Singh V, Araghi A and Tafazolli R** (2020) Sub-6 GHz dual-band 8 × 8 MIMO antenna for 5G smartphones. *IEEE Antennas and Wireless Propagation Letters* **19**(9), 1546–1550.
42. **Guo J, Cui L, Li C and Sun B** (2018) Side-edge frame printed eight-port dual-band antenna array for 5G smartphone applications. *IEEE Transactions on Antennas and Propagation* **66**(12), 7412–7417.
43. **Zou H, Li Y, Sim C-Y-D and Yang G** (2018) Design of 8 × 8 dual-band MIMO antenna array for 5G smartphone applications. *International Journal of RF and Microwave Computer-Aided Engineering* **28**(9), e21420.

https://doi.org/10.1017/S1759078724001181 Published online by Cambridge University Press

44. **Zou H *et al.*** (2019) Dual-functional MIMO antenna array with high isolation for 5G/WLAN applications in smartphones. *IEEE Access* **7**, 167470–167480.
45. **Wang H, Zhang R, Luo Y and Yang G** (2020) Compact eight-element antenna array for triple-band MIMO operation in 5G mobile terminals. *IEEE Access* **8**, 19433–19449.
46. **Pozar DM** (2012) *Microwave Engineering*, 4th Edn. Hoboken, NJ: Wiley.
47. **Thummaluru SR, Ameen M and Chaudhary RK** (2019) Four-p[ort MIMO cognitive radio system for midband 5G applications. *IEEE Transactions on Antennas and Propagation* **67**(8), 5634–5645.
48. **Sharawi MS** (2013) Printed multi-band MIMO antenna systems and their performance metrics [Wireless Corner]. *IEEE Antennas and Propagation Magazine* **55**(5), 218–232.
49. **Dey S and Dey S** (2024) Wideband highly efficient eight element MIMO antenna using differential fed open end slot for sub-7 GHz 5G mobile handset applications. *IEEE Transactions on Circuits and Systems II: Express Briefs* **71**(8), 3760–3764.

Soumik Dey is a student member of IEEE and and is currently pursuing his Ph.D. degree at the Department of Electrical Engineering, Indian Institute of Technology (IIT) Palakkad. He earned his B.Sc. in Physics (Honours) from Ramakrishna Mission Residential College, Narendrapur, in 2012, followed by B.Tech. and M.Tech. degrees in Radio Physics and Electronics from the University of Calcutta in 2016 and 2018, respectively. From December 2018 to June 2019, he worked as a research staff at IIT Palakkad before beginning his PhD in July 2019. He is a recipient of the DST Inspire Fellowship from the Government of India and the IEEE Antennas and Propagation Society Fellowship (APSF) in 2023. He also secured the first rank during his M.Tech. Programme at the University of Calcutta. He has published more than 40 research papers in international journals and conferences and filed three Indian patents. Additionally, he served as the vice-chair and chair of the IEEE AP-S Student Branch Chapter at IIT Palakkad from 2022 to 2023. His current research interests include broadband and multiband antennas, frequency-selective surfaces, metamaterials, electromagnetic bandgap structures, MIMO antennas, phased arrays, passive beamforming networks, and substrate-integrated waveguides.

Sukomal Dey received the B.Tech. degree in electronics and communication engineering from the West Bengal University of Technology, Kolkata, India, in 2006, the M.Tech. degree in mechatronics engineering from the Indian Institute of Engineering Science and Technology, Shibpur, India, in 2008, and the Ph.D. degree from the Centre for Applied Research in Electronics, Indian Institute of Technology Delhi, New Delhi, India, in July 2015. From August 2015 to July 2016, he was a Project Scientist with Industrial Research and Development Centre, IIT Delhi, and also worked on a collaborative research project supported by Synergy Microwave Corp., Paterson, NJ, USA. From August 2016 to June 2018, he was with Radio Frequency Microsystem Lab, National Tsing Hua University, Taiwan, as a Postdoctorate Research Fellow. Dr. Dey served as an Assistant Professor from June, 2018 to June 2023, and since June 2023, he has been an Associate Professor with the Department of Electrical Engineering, Indian Institute of Technology Palakkad, Kerala, India. For his M.Tech. dissertation (one year), he was with Central Electronics Engineering Research Institute, Pilani, India, in 2009. He has authored or coauthored more than 150 research papers, two state-of-the art books, two book chapters, and filed 16 patents. His research interests include electromagnetic metamaterial structures, frequency selective surfaces, microwave imaging, and microwave-integrated circuits, including antennas and RFMEMS. Dr. Dey was the recipient of the Postgraduate Student Award from the Institute of Smart Structure and System, Bangalore, India, in 2012, Best Industry Relevant Ph.D. Thesis Award from the Foundation for Innovation in Technology Transfer, IIT Delhi, in 2016, Distinction in Doctoral Research – 2016 from IIT Delhi, Postdoctoral Fellow Scholarships from the Ministry of Science and Technology, Taiwan, in 2016 and 2017, respectively, Early Career Research Award from the Science and Engineering Research Board (SERB), Government of India, in 2019, Smt. Ranjana Pal Memorial Award (2021) from the Institution of Electronics and Communication Engineers, Technology Translation Award - 2023 from SERB, India and several best paper awards with his students from national and international IEEE conferences. He has been inducted in the technical program committee 4 and 6 of the IEEE MTT Society. Dr. Dey is Senior member of IEEE, Fellow of IETE, India and current Vice-Chairman of the IEEE-MTTs society, Kerala chapter, India.

https://doi.org/10.1017/S1759078724001181 Published online by Cambridge University Press